

UC San Diego

UC San Diego Previously Published Works

Title

Modeling of carbon and tungsten transient dust influx in tokamak edge plasma

Permalink

<https://escholarship.org/uc/item/7496w7gk>

Journal

Physics of Plasmas, 30(5)

ISSN

1070-664X

Authors

Smirnov, RD

Krasheninnikov, SI

Publication Date

2023-05-01

DOI

10.1063/5.0144529

Copyright Information

This work is made available under the terms of a Creative Commons Attribution-NonCommercial-NoDerivatives License, available at

<https://creativecommons.org/licenses/by-nc-nd/4.0/>

Peer reviewed

Modeling of carbon and tungsten transient dust influx in tokamak edge plasma

R.D. Smirnov* and S.I. Krasheninnikov

*University of California San Diego, Department of Mechanical and Aerospace Engineering,
La Jolla, CA 92093*

Abstract

The paper presents computer simulation studies of burst injection of carbon and tungsten dust particles in DIII-D like edge plasmas. The injection causes a large transient influx of the low- and high-Z impurities associated with the dust ablation in the plasmas. The dust transport and the effects of the ablated impurities on the edge plasma dynamics in a modern mid-size tokamak geometry are investigated for low- and high-power plasma discharge conditions. The core plasma contamination with dust ablated impurities and the factors affecting it are evaluated.

1. Introduction

Plasma impurities, both low- and high-Z, have critical impact on performance of magnetic fusion devices due to radiative power dissipation and various elementary processes affecting plasma transport in the core and edge plasma regions. Plasma erosion of high-Z metallic plasma-facing components is usually attributed as a source of high-Z impurities in tokamaks, while low-Z impurities in addition to the “natural” production by erosion can also be intentionally injected in tokamak divertor to induce plasma detachment (e.g. see [1-3] and the references therein). While in carbon-wall machines strong erosion provides quantities of carbon impurities capable to produce significant radiative power, in all-metal wall tokamaks designed with high-Z divertor plasma facing materials (like AUG, JET-ILW, and future reactor ITER) that have relatively small erosion rate, this source of impurities is comparatively small. Consequently, the impurity radiation power loss needed to achieve detachment can only be created by the deliberate injection of impurities. For this purpose, gas-puff of nitrogen, neon, or argon into edge plasma are commonly performed in experiments on current tokamaks. The same gases are planned to be used in ITER in order to increase the radiative power dissipation in divertor volume and establish semi-detached divertor plasma conditions [3]. Also, the use of other impurities (e.g. methane, boron, etc.) is also under consideration for current tokamak experiments [3-7].

Dust, as a form of impurities naturally formed due to erosion of plasma-facing materials in tokamaks, is expected to be a substantial contributor in the overall impurity source in long-pulse plasma discharges. In addition, deliberate injection of impurities in the form of solid dust or liquid droplets opens up a new possibility to facilitate and control radiative cooling of edge plasmas and divertor detachment. Such injection of impurities in the form of dust into edge plasma of various current tokamaks (e.g. DIII-D and AUG) for the purposes of edge plasma control and assisting divertor plasma detachment has been demonstrated experimentally [8-10].

* Corresponding author e-mail: rsmirnov@ucsd.edu

Impact of impurities on fusion plasmas depends on many factors, such as impurity elemental composition, parallel and cross-field transport, the location and the rate of impurity injection into plasma, which affect impurity distribution in the plasma and associated radiation energy losses. Impurities injected into plasma in the form of dust significantly differ in many of these characteristics from conventional ionized impurities [11,12]. In particular, individual dust grains contain large amounts of material producing very strong localized impurity sources while dust ablates in the plasma. Dust grains in the plasmas also acquire electric charge by absorption of plasma ions and electrons, however, charge-to-mass ratio of typically micron-sized or larger dust is very small, so the transport of dust is also very different from ionized impurities. In addition, the physical processes governing dust ablation and transport depend on many factors, such as surrounding plasma conditions, dust material, size, and injection parameters. Another important characteristic of naturally produced dust influx in fusion plasmas is its intermittent nature associated with wall material damage or mobilization of accumulated dust by transient plasma events, such as edge localized modes (ELMs) [13]. Consequently, dust effects on fusion plasmas are inherently dynamic, requiring time-dependent consideration.

Up to date, there exists very limited number of computational investigations of dust impact on fusion plasma operation [14-18]. Our previous such studies were mainly focused on injections of tungsten dust in ITER-like plasma discharges [16,17], which are not available yet for experimental studies. It was predicted that relatively small amounts of dust grains injected into magnetic fusion devices can produce strong impact on plasma parameters. To benchmark such modelled effects with experimental data that potentially can be obtained in current devices, simulations for mid-size tokamaks are needed. The DIII-D tokamak looks particularly attractive for such benchmarking because it has both carbon and tungsten based divertor targets and existing techniques to inject dust into divertor plasma using Divertor Material Evaluation System (DiMES) mounted launcher [19] and Impurity Powder Dropper (IPD) [20].

In the following sections we describe the results of the transient carbon and tungsten dust injections simulations for the DIII-D-like plasma parameters and magnetic configuration. The comparison of impact of different quantities of carbon and tungsten dust on edge plasma, core impurity accumulation, and divertor conditions evolution are simulated. The obtained results for both low- and high-Z material dust in DIII-D-like plasma can help to design experiments for benchmarking our models.

2. Modeling setup

We conducted simulations of transient dust injection in DIII-D L-mode like plasma discharges using the dust transport code DUSTT [21] and plasma fluid code UEDGE [22], which were previously coupled in fully time-dependent, two-way data exchange manner that allows self-consistent modeling of dust and plasma evolution [17]. Two low single null plasma discharge setups in DIII-D geometry were simulated – low- and high-power regimes. The computational grid covered edge plasma between magnetic flux surfaces $\Psi_{\text{norm}}=0.95$ at the core-edge interface and $\Psi_{\text{norm}}=1.06$ at the outer wall. The boundary conditions for the simulated low-

This is the author's peer reviewed, accepted manuscript. However, the online version of record will be different from this version once it has been copyedited and typeset.

PLEASE CITE THIS ARTICLE AS DOI: 10.1063/1.50144529

power plasma regime corresponded to 2 MW heat flux crossing the core-edge interface from the core (50% with electrons and 50% with ions) and the plasma density of $1 \times 10^{19} \text{ m}^{-3}$ at the interface. The high-power case had 4 MW edge heating power and $3 \times 10^{19} \text{ m}^{-3}$ plasma density at the core-edge interface. The cross-field plasma transport coefficients were uniform and the same in both cases, i.e. $D=0.3 \text{ m}^2/\text{s}$ for particle and $\chi=1.0 \text{ m}^2/\text{s}$ for heat diffusivities, respectively. Electric fields and plasma drifts were not included in the simulations due to time-dependent nature of the simulations that requires extensive computational resources. The simulated plasma consisted of hydrogen isotope deuterium and either carbon or tungsten impurities. We modelled transport of all 6 charge states of carbon ions and 14 lower charge states of tungsten ions, which we can reasonably expect to be sufficient for the DIII-D like edge electron temperatures, varied in the simulations from $\sim 0.1 \text{ eV}$ at the divertor plates to $\sim 100 \text{ eV}$ at the midplane separatrix and to $\sim 500 \text{ eV}$ at the core interface, according to collisional-radiative equilibrium models [23,24]. Both types of impurities were assumed to be non-recycling with the recycling coefficients on the wall and divertor targets set equal 0.01 for impurity ions and albedo coefficient equal 0.1 for impurity neutrals. These values are in the range of reflection coefficients for low energy $\sim 1\text{-}100 \text{ eV}$ carbon and tungsten particles impacting on the corresponding surface at $\sim 45^\circ$ angle of incidence [25]. The sputtering of plasma-facing material surfaces both by hydrogen and impurity species was included in the UEDGE simulations. The hydrogen ion recycling coefficient was equal 1.0 on all material surfaces, assuming that they are saturated with implanted hydrogen, while hydrogen pumping was simulated by using hydrogen gas albedo coefficient 0.99 on private flux (PF) and outer walls. We assumed the initial density of impurities in the volume as well as at the core-edge interface to be negligible. In this way, the main impurity source was due to ablation of injected dust in the plasma, while the diffusive influx of impurities through the core-edge boundary allowed to evaluate core impurity content, where the core plasma itself was not simulated.

The carbon and tungsten dust grains of $10 \text{ }\mu\text{m}$ diameter were injected into the low- and high-power plasma discharges from the outer divertor strike-point location in a burst of $\tau=1 \text{ ms}$ duration, which was shaped with $\sin^2(\pi t/\tau)$ time profile of dust mass influx. The simulated total injected dust mass varied as 1, 10, and 100 mg. The initial speed of dust grains was distributed according to Maxwellian with 10 m/s average value and cosine angle distribution relative to the divertor plate normal direction. We evaluate there are $\sim 10^6$ of carbon and $\sim 10^5$ of tungsten dust grains of $10 \text{ }\mu\text{m}$ diameter per 1 mg of injected dust mass. Taking into account that the Debye length for the divertor plasma conditions is of order of microns, even for the largest number of dust grains injected ($\sim 10^8$) the grains can be considered non-interacting directly with each other at distances larger than a few mm from the injection location. Given that the injection velocities of dust grains are $\sim 10 \text{ m/s}$, it would take the grains $\sim 0.1 \text{ ms}$ to cross such distance. Therefore, the approximation of non-interacting grains can be used on the simulated spatial and temporal scales. The dust grains colliding with the walls were assigned 50% probability of sticking to the surface and 50% chance to be reflected with the normal restitution coefficient equal 0.35. These dust-wall collision parameters in ball park correspond to the theoretical estimates and

experimental measurements for the dust grains of ~ 10 -micron size and impact velocities of order of tens of m/s [26-29]. The initial temperature of dust material was assumed to be equal to the wall temperature at 400K. The dust ablation models used in the simulations included effects of shielding by ablation cloud, which for tungsten was implemented according to the high-Z ablatant shielding model developed in Refs. [30,31] and for carbon an *ad hoc* constant shielding coefficient was used that is consistent with the experimental observations [14]. From the total of 12 considered simulation cases for the different plasma and dust injection parameters, one corresponding to 100 mg of carbon dust injection in the high-power discharge has failed to converge plasma solutions due to very large localized perturbations induced by carbon impurity source and is omitted from further consideration.

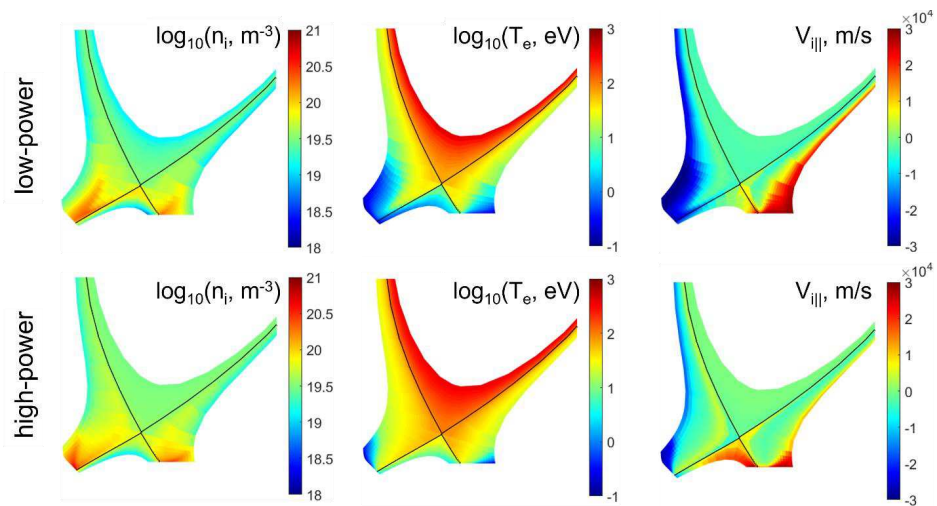


Fig. 1 Poloidal profiles of plasma density (left), electron temperature (middle), and ion parallel velocity (right) for the simulated low-power (top) and high-power (bottom) discharge cases. Positive ion velocity corresponds to poloidal direction toward the outer divertor plate.

The initial poloidal plasma ion density n_i , electron temperature T_e , and ion parallel velocity V_{\parallel} profiles, before the dust injection, are plotted for reference in Fig. 1 for the low- and high-power discharge cases. In the low-power case the inner divertor plasma is detached and the outer one is semi-detached with T_e at the inner and outer strike points equal 0.14 eV and 4.3 eV, respectively. In the high-power case, the inner divertor is semi-detached and the outer is attached with the corresponding strike point T_e equal 6.3 eV and 25 eV, respectively. We note hollowed profiles of the ion parallel velocity in scrape-off-layer (SOL) region. In the low-power discharge case there is much wider zone of large plasma speed in the SOL periphery near the divertor plates, where the plasma pressure becomes very low. Interestingly, in the high-power case relatively large plasma flows are observed in the PF region with a stagnation point in the inner

This is the author's peer reviewed, accepted manuscript. However, the online version of record will be different from this version once it has been copyedited and typeset.

PLEASE CITE THIS ARTICLE AS DOI: 10.1063/5.0144529

divertor, which can be associated with PF plasma pressure gradient developed due to plasma transport across the longer inner divertor separatrix leg as compared to the outer one. In the low-power case the inner divertor is deeply detached that effectively reduces the PF pressure asymmetry. The highlighted differences of the plasma parameters between the discharges result in important effects on the dust transport due to impact on dust ablation and acceleration by the plasmas.

3. Results

The obtained results show substantial differences in dynamics of injected carbon and tungsten impurities in the edge plasma in the different plasma regimes. First, we consider temporal evolution of the total plasma impurity content integrated over the simulated edge volume, plotted in Fig. 2. It shows that the temporal profiles of carbon impurities in low-power case and tungsten impurities in high-power case have more peaked character with relatively short period of near maximum values followed by gradual decline of the edge plasma impurity content. In contrast, the profiles for carbon dust in high-power case and for tungsten in low-power one have more broad plateau shape. We note that all plotted profiles widen with larger amount of injected impurities and that quantity of ablated tungsten impurities in the plasma start to rise earlier and more gradually compared to carbon. To understand such dynamics, we consider coupled propagation of the injected dust and evolution of the edge plasma parameters.

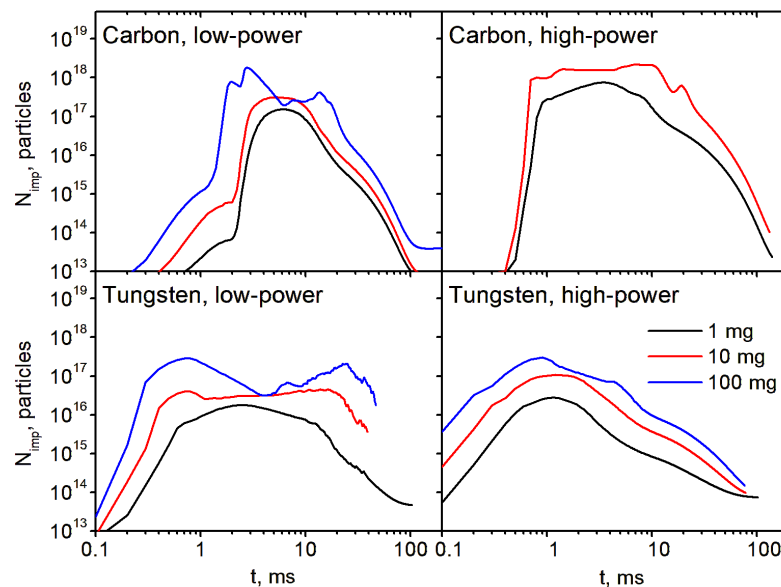


Fig. 2 Time evolution of the total impurity content integrated over the edge plasma volume for the different simulated dust injection cases.

This is the author's peer reviewed, accepted manuscript. However, the online version of record will be different from this version once it has been copyedited and typeset.

PLEASE CITE THIS ARTICLE AS DOI: 10.1063/1.50144529

Fig. 3 shows poloidal profiles of the impurity sources from dust ablation plotted at the different times for the four combinations of the injected dust material (carbon or tungsten) and the plasma cases (low- or high-power). It can be seen from comparison of this and Fig. 2 that existence of the plateau phase corresponds to the cases where dust crosses the separatrix into the core plasma region, e.g., see Fig. 3 panels corresponding to 10 ms time. The dynamics with peaked impurity content, on the contrary, correspond to the cases where dust ablates in the scrape-off-layer. The differences in the carbon and tungsten dust dynamics can be attributed to effects of plasma flows in the SOL. Carbon dust of the same size is much lighter than tungsten one and experience larger acceleration by the parallel plasma flows in the low-power discharge case, resulting in tendency of the carbon dust to be driven toward the outer wall by the centrifugal force. The tungsten dust in this case is much less affected by the centrifugal acceleration and continues to spread toward the core and inner divertor inertially, see Fig. 3 (top two rows). In the high-power case the plasma velocities are low in most of the SOL volume, resulting in dust ablation rate to be a more important factor in the ability of dust to reach the core plasma. Further illustrating the differences in plasma contamination with dust material is the fraction of total injected dust mass ablated in the plasma, shown in Table 1 for all simulated dust injection cases. Due to the centrifugal acceleration, as described above, most carbon dust grains are not fully ablated and stick to the wall in the low-power discharge. Notably, ablated mass fraction of tungsten dust increases with the total mass injected in low-power case and significantly decreases in the high-power one. Also, for the low injected mass of tungsten dust it appears to ablate faster than carbon one in the high-power case, despite carbon and tungsten having similar enthalpy of vaporization. The reason for this can be related to the difference in shielding models for carbon and tungsten dust, as well as to how the dust ablated impurities affect divertor plasma conditions, which will be discussed further in the paper.

This is the author's peer reviewed, accepted manuscript. However, the online version of record will be different from this version once it has been copyedited and typeset.

PLEASE CITE THIS ARTICLE AS DOI: 10.1063/5.0144529

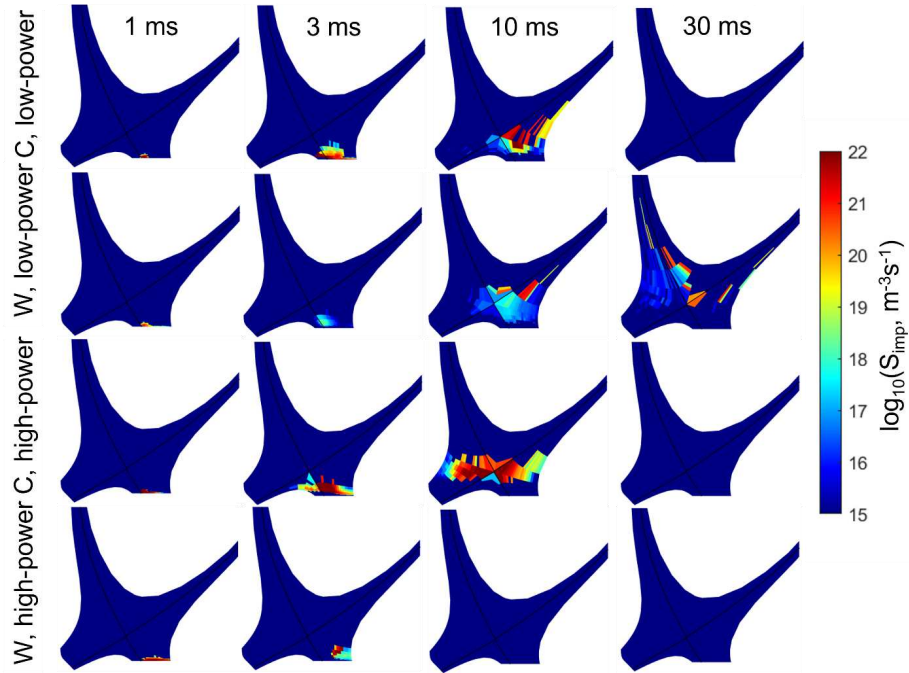


Fig. 3 Profiles of dust ablation impurity source at 1, 3, 10, and 30 ms time after dust burst start (columns from left to right) for 100 mg of carbon (first row) or tungsten (second row) dust injected in low-power plasma; 10 mg of carbon (third row) or 100 mg of tungsten (fourth row) dust injected in the high-power plasma case.

Injected dust mass	C, low-power	C, high-power	W, low-power	W, high-power
1 mg	0.042	0.635	0.756	0.982
10 mg	0.015	0.560	0.820	0.543
100 mg	0.048	-	0.924	0.284

Table 1 Fraction of total injected dust mass ablated in the plasma volume.

To understand impact of injected dust on the plasmas we consider profiles of impurity concentrations plotted in Fig. 4 for the same cases and time moments as in Fig. 3. Comparing the two figures one can see that within few ms of dust injection the source of ablated impurities is localized near the injection position in the outer divertor following relatively slow dust grains, which can propagate to distance of a few cm during this time. Simultaneously, the impurities introduced in the plasma due to dust ablation has already spread through the edge plasma including the core. This signifies importance of impurity transport in assessing dust effects on the fusion plasmas, as it is much faster in comparison to dust dynamics. We estimate the neutral impurity ionization mean free path to be of order of 1 cm under the high-power divertor plasma

This is the author's peer reviewed, accepted manuscript. However, the online version of record will be different from this version once it has been copyedited and typeset.

PLEASE CITE THIS ARTICLE AS DOI: 10.1063/5.0144529

conditions. Also, for the simulated cross-field diffusivity of $0.3 \text{ m}^2/\text{s}$, the ionized impurities at 1 ms time could propagate only to $\sim 2 \text{ cm}$ distance in perpendicular to the magnetic field direction. However, we can see in Fig. 4 that the concentration of impurities in the core region is already large on this time scale. We, therefore, must conclude that the path of impurity penetration to the core region lays through an upstream SOL region above the X-point, where the magnetic field surfaces are more condensed spatially. This is consistent with the much faster impurity transport along the magnetic field lines, which can roughly be estimated by the impurity ion sound speed of order of $\sim 10^4 \text{ m/s}$.

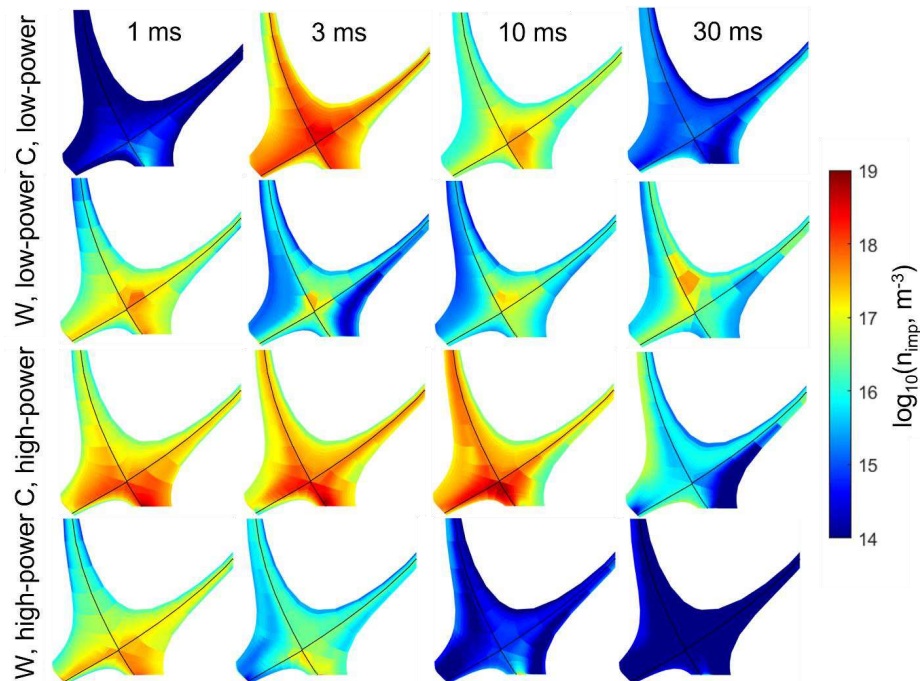


Fig. 4 Profiles of impurity concentration at 1, 3, 10, and 30 ms time after dust burst start (columns from left to right) for 100 mg of carbon (first row) or tungsten (second row) dust injected in low-power plasma; 10 mg of carbon (third row) or 100 mg of tungsten (fourth row) dust injected in the high-power plasma case.

Thus, parallel impurity transport plays critical role in the penetration of dust ablated impurities to the core plasma. Fig. 5 shows profiles of the poloidal flux of impurities for the same simulated cases and time moments as in Figs. 3 and 4. The forces affecting parallel impurity propagation are the impurity pressure gradient force, plasma ion drag force, neutral friction and the ion thermal forces. Among these, the pressure gradient and the thermal forces are

This is the author's peer reviewed, accepted manuscript. However, the online version of record will be different from this version once it has been copyedited and typeset.

PLEASE CITE THIS ARTICLE AS DOI: 10.1063/1.50144529

the main contributors to impurity spreading upstream, while the ion drag by the plasma flows toward the divertor plates (see Fig. 1) would tend to confine impurities in the divertor volume. As these forces are radially inhomogeneous due to the large radial plasma density and temperature gradients existing in SOL, the interplay between the parallel forces and impurity radial diffusion produces striated impurity structures in the edge, Fig. 5. As can be seen in this figure, in the low-power discharges there is narrow channel in the outer mid-SOL region, where dust ablated impurities propagate upstream. The impurity flow near the separatrix and in the far SOL is dominated by ion drag force toward the divertor target. In the high-power case the upstream impurity channel is much wider and is more persistent due to higher divertor plasma pressure. As the dust and the peak of corresponding ablated impurity source propagate with time away from the outer divertor plate (Fig. 3), so the stagnation curve in poloidal plane dividing the upstream-downstream impurity fluxes shifts upstream (Fig. 5). Notably, the stagnation curve in SOL is radially very non-monotonic, reflecting poloidally shifting balance of the forces acting on impurities at different radial locations.

In addition, the drifts, which were not included in these simulations, can affect the patterns of plasma flows in the SOL, so affecting the ion drag force on the dust grains and ablated material. The drifts of impurity ions can also play a role in their spreading upstream. Depending on direction of the magnetic field, drifts potentially can both assist or inhibit dust and ablated impurities propagation out of the divertor volume.

Moreover, comparing Fig. 4 and Fig. 1 we see that the impurity concentrations can reach a significant fraction of plasma density near the separatrix in the divertor region. This can cause, besides the radiative plasma cooling, increased divertor target material sputtering by heavy impurity ions.

This is the author's peer reviewed, accepted manuscript. However, the online version of record will be different from this version once it has been copyedited and typeset.

PLEASE CITE THIS ARTICLE AS DOI: 10.1063/5.0144529

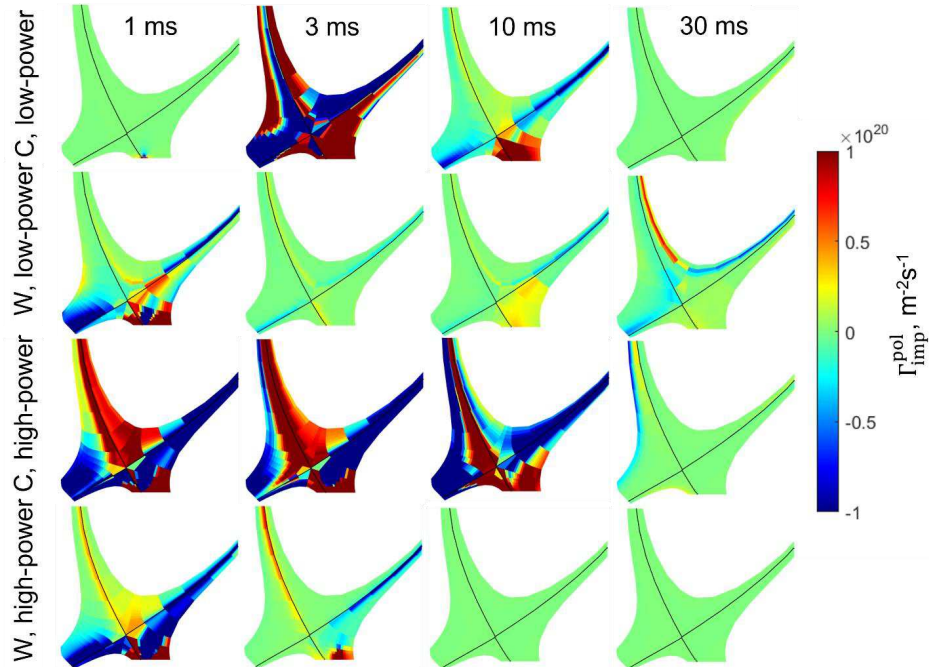


Fig. 5 Profiles of poloidal flux of impurities at 1, 3, 10, and 30 ms time after dust burst start (columns from left to right) for 100 mg of carbon (first row) or tungsten (second row) dust injected in low-power plasma; 10 mg of carbon (third row) or 100 mg of tungsten (fourth row) dust injected in the high-power plasma case. Positive poloidal flux direction is from the inner to the outer divertor plates.

We note, that as the core-edge boundary conditions in these simulations presume negligibly small impurity concentration, the impurities crossing the separatrix further diffuse into the central core region not covered by the grid. This allows us to evaluate core impurity accumulation and the approximate core impurity concentration, while the core plasma itself is not simulated. As a tradeoff, it also leads to eventual diminishing of impurities in the simulated core-edge plasma volume after the injected dust is fully ablated, as seen in Fig. 4. Consequently, the impurity concentration is maintained in the core-edge region while the dust ablates there, see Fig. 4 the second and the third rows.

This is the author's peer reviewed, accepted manuscript. However, the online version of record will be different from this version once it has been copyedited and typeset.

PLEASE CITE THIS ARTICLE AS DOI: 10.1063/1.50144529

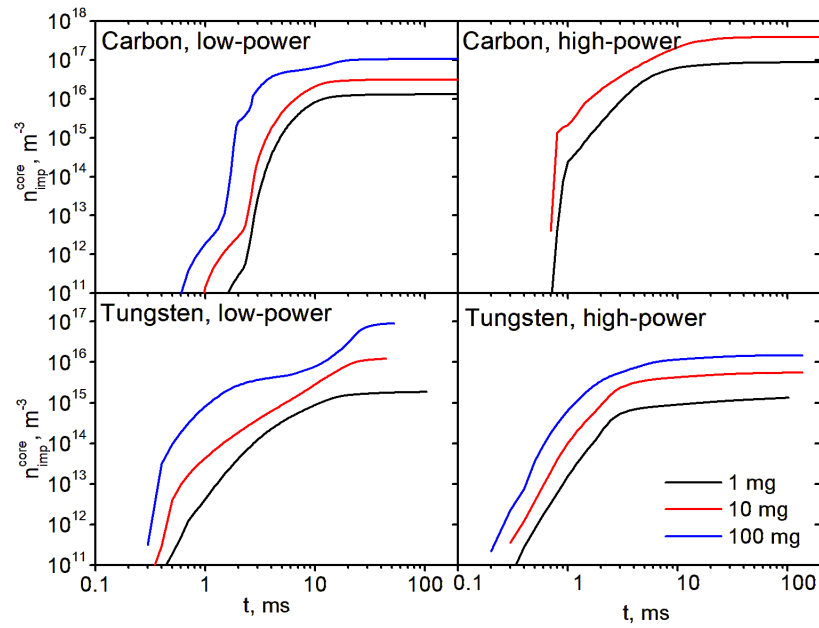


Fig. 6 Estimated accumulated core impurity concentration for the different simulated dust injection cases.

Injected dust mass	C, low-power	C, high-power	W, low-power	W, high-power
1 mg	1.3e-3	2.9e-3	1.9e-4	4.4e-5
10 mg	3.1e-3	1.3e-2	1.2e-3	1.9e-4
100 mg	1.1e-2	-	8.9e-3	4.9e-4

Table 2 Evaluated maximum core impurity fraction for the various simulated dust injection scenarios.

The core impurity concentration can be evaluated by integrating in time of the impurity fluxes crossing the core-edge interface and dividing it by the core region volume, which is equal 14.5 m^3 for the simulated geometry. This presumes that the impurities entering the core region are retained there and, therefore, the calculated in such way core impurity concentration can serve as an upper limit estimate. Fig. 6 shows time evolution of the estimated core impurity concentrations for the different simulated dust injection scenarios. One can see from the Fig. 6 that the core impurity content reaches the near saturation levels within time from several ms to a few tens of ms that corresponds to the end of the peak/plateau phase of impurity content in the edge plasma. The saturation values of the core impurity concentration increase with the amount of the injected dust. However, the dependencies are weaker than linear with power law exponents equal 0.45 and 0.65 for carbon, 0.84 and 0.52 for tungsten in low- and high-power

regimes, respectively. Assuming plasma core density is the same as at the core-edge boundary and equal $1 \times 10^{19} \text{ m}^{-3}$ for the low-power and $3 \times 10^{19} \text{ m}^{-3}$ for the high-power cases, we estimate the maximum core impurity fraction given in Table 2. For the cases, where dust crosses the separatrix, the table shows extremely high core impurity fractions, which would lead to the radiative plasma collapse. In the case of tungsten dust injection in the high-power discharge, when the dust does not cross the separatrix, the core impurity fraction reaches values $\sim 10^{-4}$, which still can have critical impact on the core plasma performance [32]. We also note that accumulated impurity content of the core, corresponding to Fig. 6 and Table 2, represents only a very small fraction of the total impurity atoms ablated from dust in the plasma, which varies from 0.014% to 0.62% for the simulated cases.

The simulated in UEDGE impurity-induced plasma cooling includes line radiation and binding energy losses due to impurity excitation, recombination, and ionization. The energy losses due to dust material vaporization are not included in the plasma modeling, as the vaporization energy per carbon or tungsten atom is generally small in comparison to the energy loss on multiple ionizations and radiation per impurity atom during its residence in the fusion plasmas. The total impurity radiated power in the simulated edge plasmas evolves in time similarly to the total plasma impurity content plotted in Fig. 2. The peak values of the impurity radiated power are given in Table 3. As one can see, in the high-power cases the injection of tungsten dust can lead to lower radiated power than carbon dust, due to the fact that there are ~ 15 times more carbon than tungsten atoms corresponding to the same dust mass. Notably, the peak impurity radiation power losses even can transiently exceed the total edge plasma heating power for the large quantities of injected dust material leading to substantial plasma cooling.

Injected dust mass	C, low-power	C, high-power	W, low-power	W, high-power
1 mg	0.22	1.80	0.42	1.39
10 mg	0.50	4.20	0.88	2.73
100 mg	2.53	-	3.30	5.06

Table 3 Peak impurity radiated power (MW) in the whole edge plasma volume for the various simulated dust injection scenarios.

This is the author's peer reviewed, accepted manuscript. However, the online version of record will be different from this version once it has been copyedited and typeset.

PLEASE CITE THIS ARTICLE AS DOI: 10.1063/5.0144529

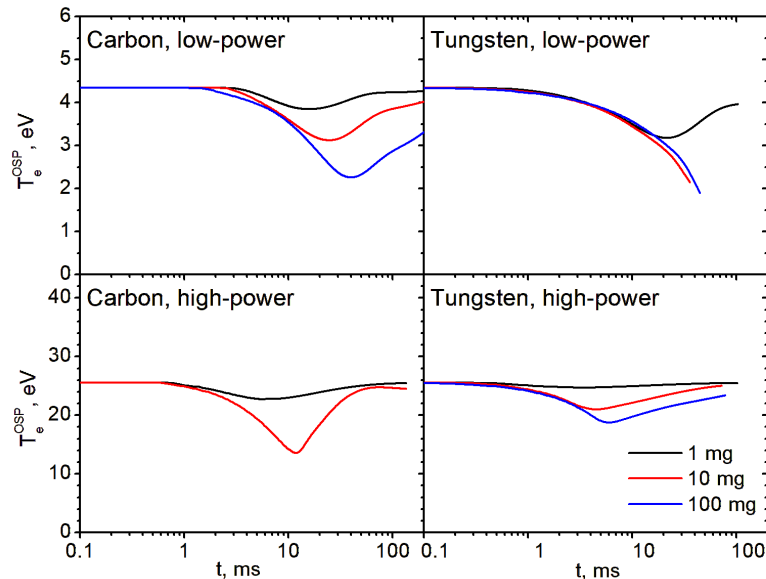


Fig. 7 Evolution of the electron temperature at the outer divertor strike point for the simulated dust injection scenarios.

As was indicated above, the rate of dust ablation plays defining role in dust's ability to propagate deeper into the plasma in the high-power plasma case, where the parallel plasma flows are relatively weak. The dust ablation rate is directly affected by the plasma parameters, which can also evolve in response to the influx of ablated impurities. The evolution of the electron temperature at the outer divertor strike point is shown in Fig. 7. As expected, influx of ablated impurities leads to transient decrease of the electron temperature due to impurity radiation plasma cooling. It is interesting to see, however, that the temperature reduction due to injection of the same mass of tungsten dust is stronger than that of carbon dust in the low-power discharge and weaker in the high-power one. The observed amplitude of the electron temperature reduction is correlated with the ability of dust grains to reach the plasma core. The electron temperature drop reduces dust ablation rate in the divertor plasma and facilitates its penetration to the core region. This increases plasma volume where dust-introduced impurities radiate, thus, enhancing cooling effect on the edge plasma conditions. Such feedback mechanism further amplifies differences in the carbon and tungsten dust ablation in the divertor, which could initially be produced by the differences in the models of dust shielding by ablation cloud.

The dust injection also affects the upstream plasma conditions. Fig. 8 shows the variation in time of the electron temperature at the mid-plane separatrix. We can see that in the low-power case the upstream temperature is weakly affected by the low doses of injected dust. The upstream plasma cooling becomes significant for the large, ~ 100 mg, mass of injected dust and when the

tungsten dust crosses the separatrix. In the high-power case, the mid-plane electron temperature is less sensitive to the dust injection than in the low-power one, and even can increase slightly, while the divertor temperature always decreases following dust injection, as we saw in Fig. 7.

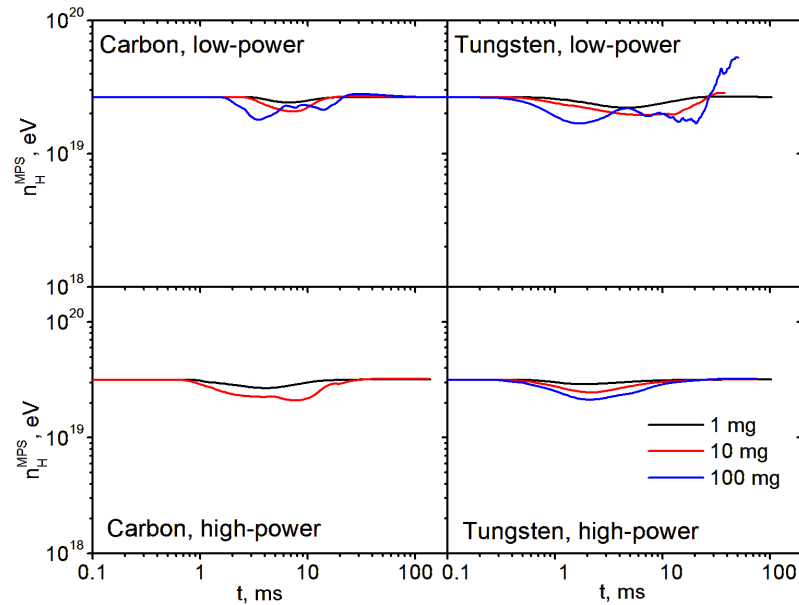


Fig. 8 Variation in time of the electron temperature at the mid-plane separatrix for the simulated dust injection cases.

Such temperature increase can be understood considering dynamics of SOL plasma induced by radiative plasma cooling from injected dust impurities. Simultaneously with the substantial divertor temperature drop (Fig. 9a), the plasma pressure in the divertor region also decreases causing pressure drop throughout the edge (Fig. 9b). This leads to reduction of the upstream electron density (Fig. 9c) and subsequently decreases the *anomalous cross-field* thermal conductivity, which is proportional to electron density, while the *parallel* thermal conductivity is assumed classical and density independent. The decrease of the cross-field heat conductivity causes the radial gradient of the electron temperature to grow, Fig. 9(d).

The radial gradient steepening together with the increasing downstream impurity-induced power losses cause the peaks of radial profiles of the electron poloidal heat flux at the outer mid-plane, shown in Fig. 10, to increase somewhat and also shift inwards after dust injection. One can see, however, that in the high-power cases the heat flux peaks remain in the SOL, Figs. 10(c,d), while in the low-power cases the shift is very significant, so that the peaks are positioned inside the separatrix, Figs. 10(a,b), depending on relative contribution of the radiative losses in

these regimes. Consequently, in the high power cases the poloidal heat flux becomes somewhat larger and narrower near the separatrix, leading to the transient increase of the electron temperature at the mid-plane separatrix, Fig. 8. In the low-power cases, the larger shift generally leads to decrease of the poloidal heat flux and the electron temperature at the separatrix.

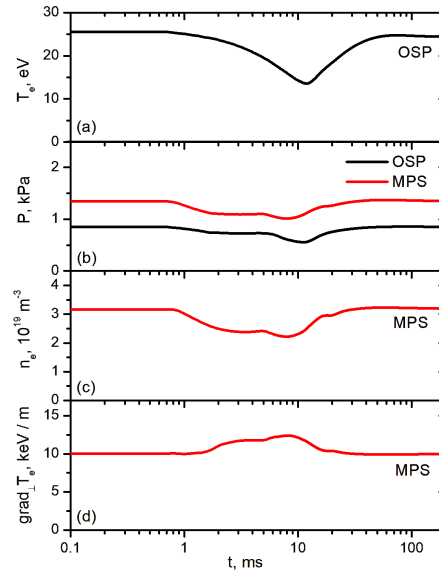


Fig. 9 Time evolution of electron temperature at OSP (a); total plasma pressure at OSP and MPS (b); MPS electron density (c); and radial gradient of electron temperature at MPS (d) for 10 mg of carbon dust injected in the high-power plasma. Here, OSP means outer strike point and MPS means outer mid-plane separatrix location.

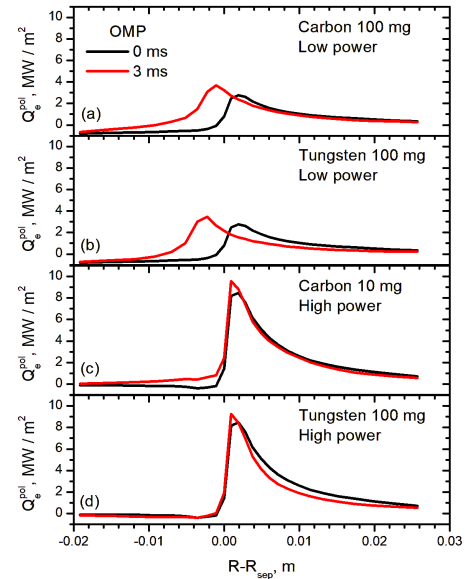


Fig. 10 Radial profiles of the poloidal electron heat flux at the outer midplane (OMP) for injected (a) 100 mg of C and (b) W dust in low-power case; (c) 10 mg of C and (d) 100 mg of W dust in high-power case at before (0 ms) and 3ms after start of the injection.

4. Conclusions

Effects of transient carbon and tungsten dust injection on the edge plasmas of a medium size tokamak were studied using time-dependent simulations with DUSTT/UEDGE coupled codes. The simulations were performed for low- and high-power plasma regimes in DIII-D like geometry. The amounts of 10 μm diameter dust injected in the outer divertor for the both materials varied as 1, 10, and 100 mg. The simulations demonstrate that in medium size tokamaks the ability of dust to reach the core plasma from outer divertor strongly depends on pattern and strength of plasma flows in the SOL and the dust inertia. In particular, strong plasma

This is the author's peer reviewed, accepted manuscript. However, the online version of record will be different from this version once it has been copyedited and typeset.

PLEASE CITE THIS ARTICLE AS DOI: 10.1063/1.50144529

flows in the low-power discharges can cause significant acceleration of carbon dust toroidally and hinder its ability to penetrate into the core due to action of the centrifugal force. While in the high-power plasma regime and for tungsten dust the possibility for dust to reach the core plasma is mainly controlled by dust ablation rate in the surrounding plasma. The simulations also show that while magnitude of impact of dust injection on edge plasma parameters is mainly controlled by amount of dust and is similar for both carbon and tungsten, the duration of the effects is longer in the cases when the dust can enter the core region. We also found that dust injection causes prompt contamination of the core plasma with impurities in early stages of dust ablation even when it is localized in the divertor region. The simulations results suggest that fast parallel transport and upstream cross-field impurity diffusion are responsible for such effect rather than direct downstream spreading of dust ablated impurities from divertor to the core region. The maximum core impurity fraction produced by dust injection was evaluated, which shows that already ~ 10 mg of injected dust can cause the fraction to exceed maximum tolerable levels and the core impurity content become much larger if the dust is able to cross the separatrix into the core.

The simulations also demonstrate that injection of both carbon and tungsten dust substantially reduces divertor plasma temperatures by radiative plasma cooling, causing the plasma to detach in the low-power discharges. The cooling effect is not straightforwardly dependent on injected dust amount and material, while also depending on whether the dust can reach the core. We found that radiative plasma cooling by dust-ablated impurities has synergistic effect on the core impurity contamination, when impurities radiating in the core region further facilitate dust penetration into the core by reducing dust ablation rate in the cooler edge plasma. The effect of dust injection on upstream plasma conditions is found to be more complex, where electron temperature at outer mid-plane separatrix can transiently rise in the high-power regime due to reduction of the anomalous cross-field thermal diffusivity induced by dust injection via chain of effects in the SOL plasmas. It was found that the interplay between dust effects on the upstream cross-field thermal diffusivity and on the downstream plasma cooling led to increase and inward shift of the peak of poloidal electron heat flux, which cause narrowing of the radial electron heat flux profile in the high-power discharge SOL.

These results demonstrate that dust impact on the edge plasmas is a complex synergistic phenomenon involving the effects of inhomogeneous plasma on dust acceleration and ablation and conversely the non-local effects of ablated impurities on plasma conditions. It is important, however, to highlight that the obtained results depend on the multi-faceted models implemented in the simulation codes and need to be experimentally validated. In particular, dust shielding by the ablation cloud requires development of reliable quantitative description for the different dust materials. Moreover, it is possible that not all forces acting on dust in the inhomogeneous magnetized tokamak plasmas are currently identified and implemented in the simulation codes. However, high quality experimental data on dust dynamics in fusion devices suitable for quantitative comparison with the simulations remains scarce. To improve dust transport modeling reliability and precision, further theoretical and experimental studies are required.

This is the author's peer reviewed, accepted manuscript. However, the online version of record will be different from this version once it has been copyedited and typeset.

PLEASE CITE THIS ARTICLE AS DOI: 10.1063/1.50144529

Acknowledgements

This material is based upon the work supported by the U.S. Department of Energy, Office of Science, Office of Fusion Energy Sciences under Award No. DE-FG02-06ER54852.

Data Availability Statement

The data that support the findings of this study are available from the corresponding author upon reasonable request.

References

- [1] S. I. Krasheninnikov and A. S. Kukushkin, "Physics of ultimate detachment of a tokamak divertor plasma", *J. Plasma Phys.* **83** (2017) 155830501.
- [2] A. Loarte, R.D. Monk, J.R. Martín-Solís, D.J. Campbell, A.V. Chankin, S. Clement, S.J. Davies, J. Ehrenberg, S.K. Erements, H.Y. Guo, P.J. Harbour, L.D. Horton, L.C. Ingesson, H. Jäckel, J. Lingertat, C.G. Lowry, C.F. Maggi, G.F. Matthews, K. McCormick, D.P. O'Brien, R. Reichle, G. Saibene, R.J. Smith, M.F. Stamp, D. Stork, and G.C. Vlases, "Plasma detachment in JET Mark I divertor experiments", *Nucl. Fusion* **38** (1998) 331.
- [3] ITER Physics Basis, "Chapter 4: Power and particle control", *Nucl. Fusion* **39** (1999) 2391.
- [4] A. Kallenbach, M. Bernert, M. Beurskens, L. Casali, M. Dunne, T. Eich, L. Giannone, A. Herrmann, M. Maraschek, S. Potzel, F. Reimold, V. Rohde, J. Schweinzer, E. Viezzer, M. Wischmeier, and the ASDEX Upgrade Team, "Partial detachment of high power discharges in ASDEX Upgrade", *Nucl. Fusion* **55** (2015) 053026.
- [5] F. Reimold, M. Wischmeier, M. Bernert, S. Potzel, A. Kallenbach, H.W. Muller, B. Sieglin, U. Stroth, and the ASDEX Upgrade Team, "Divertor studies in nitrogen induced completely detached H-modes in full tungsten ASDEX Upgrade", *Nucl. Fusion* **55** (2015) 033004.
- [6] C. Guillemaut, M. Lennholm, J. Harrison, I. Carvalho, D. Valcarcel, R. Felton, S. Griph, C. Hogben, R. Lucock, G. F. Matthews, C. Perez Von Thun, R. A. Pitts, S. Wiesen, and JET contributors, "Real-time control of divertor detachment in H-mode with impurity seeding using Langmuir probe feedback in JET-ITER-like wall", *Plasma Phys. Contr. Fusion* **59** (2017) 045001.
- [7] B. Lipschultz, J. L. Terry, C. Boswell, J. A. Goetz, A. E. Hubbard, S. I. Krasheninnikov, B. LaBombard, D. A. Pappas, C. S. Pitcher, F. Wising, and S. Wukitch, "The role of particle sinks and sources in Alcator C-Mod detached divertor discharges", *Phys. Plasmas* **6** (1999) 1907.
- [8] T.H. Osborne, G.L. Jackson, Z. Yan, R. Maingi, D.K. Mansfield, B.A. Grierson, C.P. Chrobak, A.G. McLean, S.L. Allen, D.J. Battaglia, A.R. Briesemeister, M.E.

This is the author's peer reviewed, accepted manuscript. However, the online version of record will be different from this version once it has been copyedited and typeset.

PLEASE CITE THIS ARTICLE AS DOI: 10.1063/5.0144529

- Fenstermacher, G.R. McKee, P.B. Snyder, and the DIII-D Team “Enhanced H-mode pedestals with lithium injection in DIII-D”, *Nucl. Fusion* **55** (2015) 063018.
- [9] R. Lunsford, V. Rohde, A. Bortolon, R. Dux, A. Herrmann, A. Kallenbach, R. McDermott, P. David, A. Drenik, F. Laggner, R. Maingi, D.K. Mansfield, A. Nagy, R. Neu, E. Wolfrum, and the ASDEX Upgrade Team “Active conditioning of ASDEX Upgrade tungsten plasma-facing components and discharge enhancement through boron and boron nitride particulate injection”, *Nucl. Fusion* **59** (2019) 126034.
- [10] F. Effenberg, A. Bortolon, L. Casali, R. Nazikian, I. Bykov, F. Scotti, H.Q. Wang, M.E. Fenstermacher, R. Lunsford, A. Nagy, B.A. Grierson, F.M. Laggner, R. Maingi, and the DIII-D Team “Mitigation of plasma–wall interactions with low-Z powders in DIII-D high confinement plasmas”, *Nucl. Fusion* **62** (2022) 106015.
- [11] S.I. Krasheninnikov, R.D. Smirnov, and D.L. Rudakov “Dust in magnetic fusion devices”, *Plasma Phys. Control. Fusion* **53** (2011) 083001.
- [12] S. Ratynskaia, A. Bortolon, S.I. Krasheninnikov “Dust and powder in fusion plasmas: recent developments in theory, modeling, and experiments”, *Reviews of Modern Plasma Physics* **6** (2022) 20.
- [13] M. Sertoli, J.C. Flanagan, M. Bacharis, O. Kardaun, A. Jarvinen, G.F. Matthews, S. Brezinsek, D. Harting, A. Cackett, E. Hodille, I.H. Coffey, E. Lazzaro, and T. Pütterich “Impact of W events and dust on JET-ILW operation”, *Journal of Nuclear Materials* **463** (2015) 837.
- [14] R.D. Smirnov, S.I. Krasheninnikov, A.Y. Pigarov, A.L. Roquemore, D.K. Mansfield, J. Nichols, “Modeling of dust impact on tokamak edge plasmas”, *J. Nucl. Mater.* **415** (2011) S1067.
- [15] R.D. Smirnov, S.I. Krasheninnikov, A.Yu. Pigarov, T.D. Rognlien, D.K. Mansfield, C.H. Skinner, and A.L. Roquemore “Impurity Seeding with Dust injection in Tokamak Edge Plasmas”, *Contrib. Plasma Phys.* **52** (2012) 435.
- [16] R.D. Smirnov, S.I. Krasheninnikov, A.Yu. Pigarov, and T.D. Rognlien “Tungsten dust impact on ITER-like plasma edge”, *Phys. Plasmas* **22** (2015) 012506.
- [17] R.D. Smirnov and S.I. Krasheninnikov “Time-dependent modeling of dust outburst into tokamak divertor plasma”, *Phys. Plasmas* **27** (2020) 082509.
- [18] E. Lazzaro, F. Causa, G. Gervasini, F. Ghezzi, D. Borodin, I. Borodkina, D. Douai, A. Huber, E. Pawelec, E. Solano, M. Sertoli, A. Widdowson, and JET Contributors “Simulated effects of W dust ablation and deposition on the pedestal edge in JET D and DT experiments” *Nucl. Fusion* **62** (2022) 126037.
- [19] I. Bykov, D.L. Rudakov, E. Kostadinova, C. Lasnier, W. Meyer, C. Marini, A. McLean, D.M. Orlov, R.D. Smirnov, “Compact Injector for Studies of Solids Interaction with Fusion

This is the author's peer reviewed, accepted manuscript. However, the online version of record will be different from this version once it has been copyedited and typeset.

PLEASE CITE THIS ARTICLE AS DOI: 10.1063/5.0144529

- Plasmas”, the 24th Topical Conference on High Temperature Plasma Diagnostics (May 15-19, 2022, Rochester, NY), PC-29.
- [20] A. Nagy, A. Bortolon, D. M. Mauzey, E. Wolfe, E. P. Gilson, R. Lunsford, R. Maingi, D. K. Mansfield, R. Nazikian, and A. L. Roquemore “A multi-species powder dropper for magnetic fusion applications”, *Review of Scientific Instruments* **89** (2018) 10K121.
- [21] R.D. Smirnov, A.Y. Pigarov, M. Rosenberg, S.I. Krasheninnikov, D.A. Mendis “Modelling of dynamics and transport of carbon dust particles in tokamaks”, *Plasma Phys. Control. Fusion* **49** (2007) 347.
- [22] T.D. Rognlien, J.L. Milovich, M.E. Rensink, G.D. Porter “A fully implicit, time dependent 2-D fluid code for modeling tokamak edge plasmas”, *J. Nucl. Mater.* **196–198** (1992) 347.
- [23] D.E. Post, R.V. Jensen, C.B. Tarter, W.H. Grasberger, and W.A. Lokke “Steady-state radiative cooling rates for low-density, high-temperature plasmas” *At. Data Nucl. Data Tables* **20** (1977) 397.
- [24] R.A. Hulse “Numerical Studies of Impurities in Fusion Plasmas”, *Nucl. Technol.* **3** (1983) 259.
- [25] W. Eckstein “Calculated Sputtering, Reflection and Range Values”, MPI-Garching Report, IPP 9/132 (2002).
- [26] C. Thornton and Z. Ning “A theoretical model for the stick/bounce behaviour of adhesive, elastic-plastic spheres”, *Powder Technology* **99** (1998) 154.
- [27] S. Ratynskaia, L. Vignitchouk, P. Talias, I. Bykov, H. Bergs aker, A. Litnovsky, N. den Harder, and E. Lazzaro “Migration of tungsten dust in tokamaks: role of dust–wall collisions”, *Nucl. Fusion* **53** (2013) 123002.
- [28] S. Ratynskaia, P. Talias, A. Shalpegin, L. Vignitchouk, M. De Angeli, I. Bykov, K. Bystrov, S. Bardin, F. Brochard, D. Ripamonti, N. den Harder, and G. De Temmerman “Elastic–plastic adhesive impacts of tungsten dust with metal surfaces in plasma environments”, *J. Nucl. Mater.* **463** (2015) 877.
- [29] A. Shalpegin, F. Brochard, S. Ratynskaia, P. Talias, M. De Angeli, L. Vignitchouk, I. Bykov, S. Bardin, K. Bystrov, T. Morgan, and G. De Temmerman “Highly resolved measurements of dust motion in the sheath boundary of magnetized plasmas”, *Nucl. Fusion* **55** (2015) 112001.
- [30] S.I. Krasheninnikov and E.D. Marenkov “On ablation of large Tungsten dust grains in edge plasma of fusion devices”, *Journal of Nuclear Materials* **463** (2015) 869.
- [31] E.D. Marenkov and S.I. Krasheninnikov “Ablation of high-Z material dust grains in edge plasmas of magnetic fusion devices”, *Phys. Plasmas* **21** (2014) 123701.

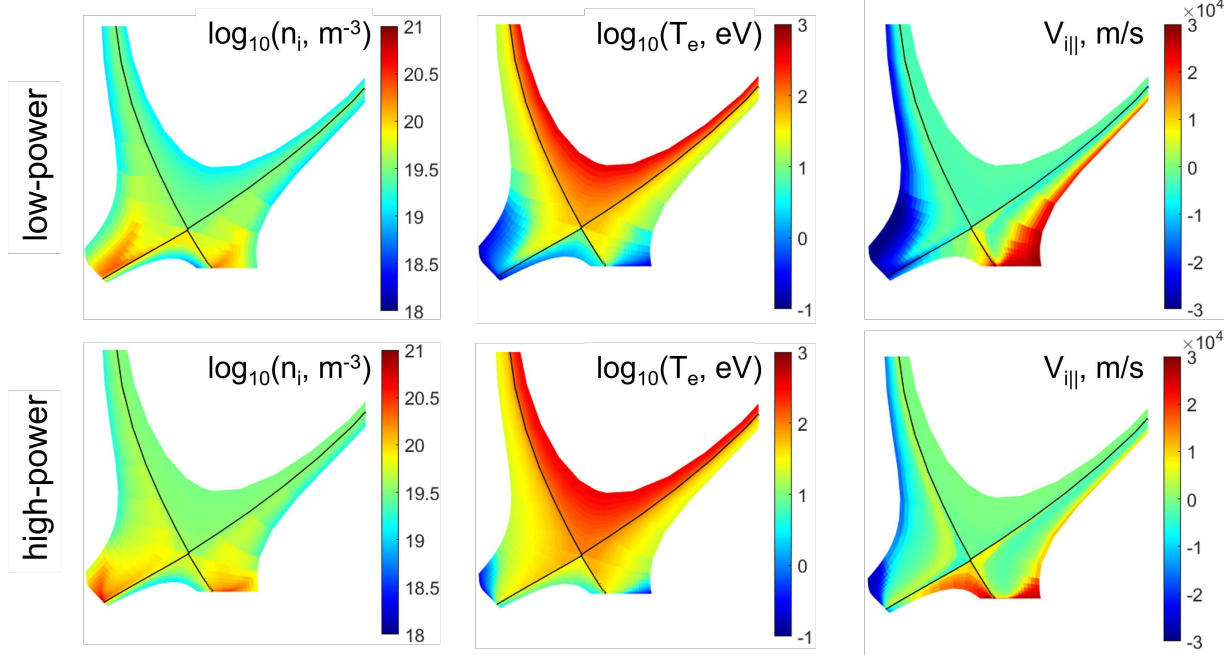
This is the author's peer reviewed, accepted manuscript. However, the online version of record will be different from this version once it has been copyedited and typeset.

PLEASE CITE THIS ARTICLE AS DOI: 10.1063/1.50144529

- [32] T. Pütterich, E. Fable, R. Dux, M. O'Mullane, R. Neu, M. Siccino "Determination of the tolerable impurity concentrations in a fusion reactor using a consistent set of cooling factors", Nucl. Fusion **59** (2019) 056013.

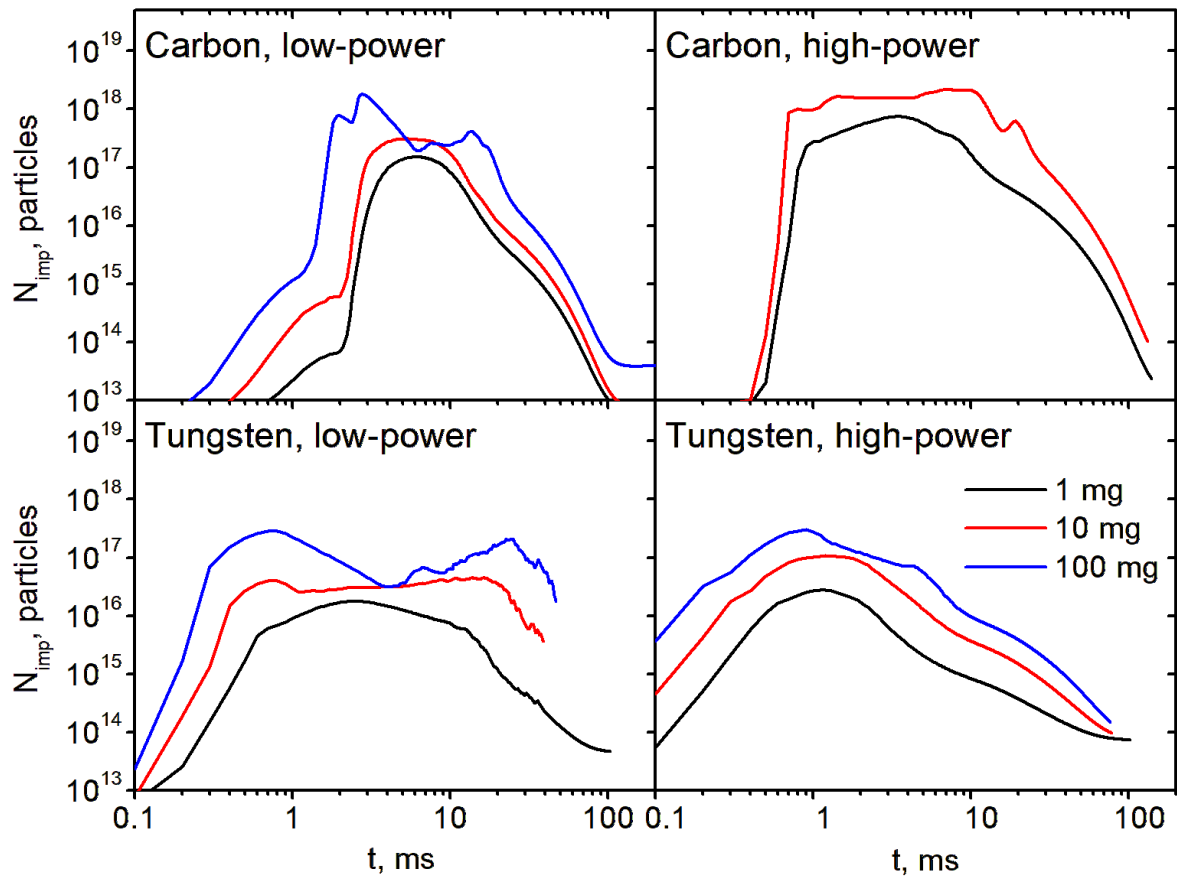
This is the author's peer reviewed, accepted manuscript. However, the online version of record will be different from this version once it has been copyedited and typeset.

PLEASE CITE THIS ARTICLE AS DOI: 10.1063/5.0144529



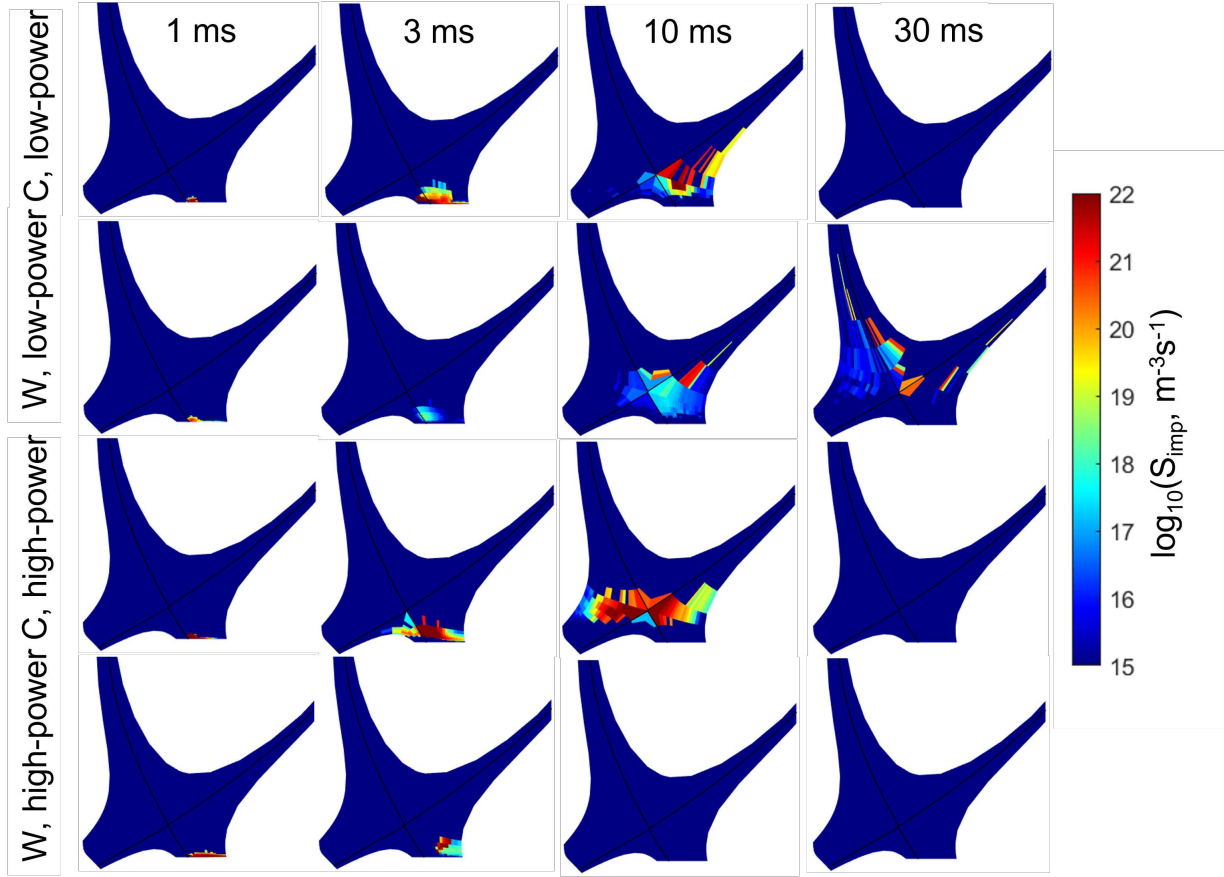
This is the author's peer reviewed, accepted manuscript. However, the online version of record will be different from this version once it has been copyedited and typeset.

PLEASE CITE THIS ARTICLE AS DOI: 10.1063/5.0144529



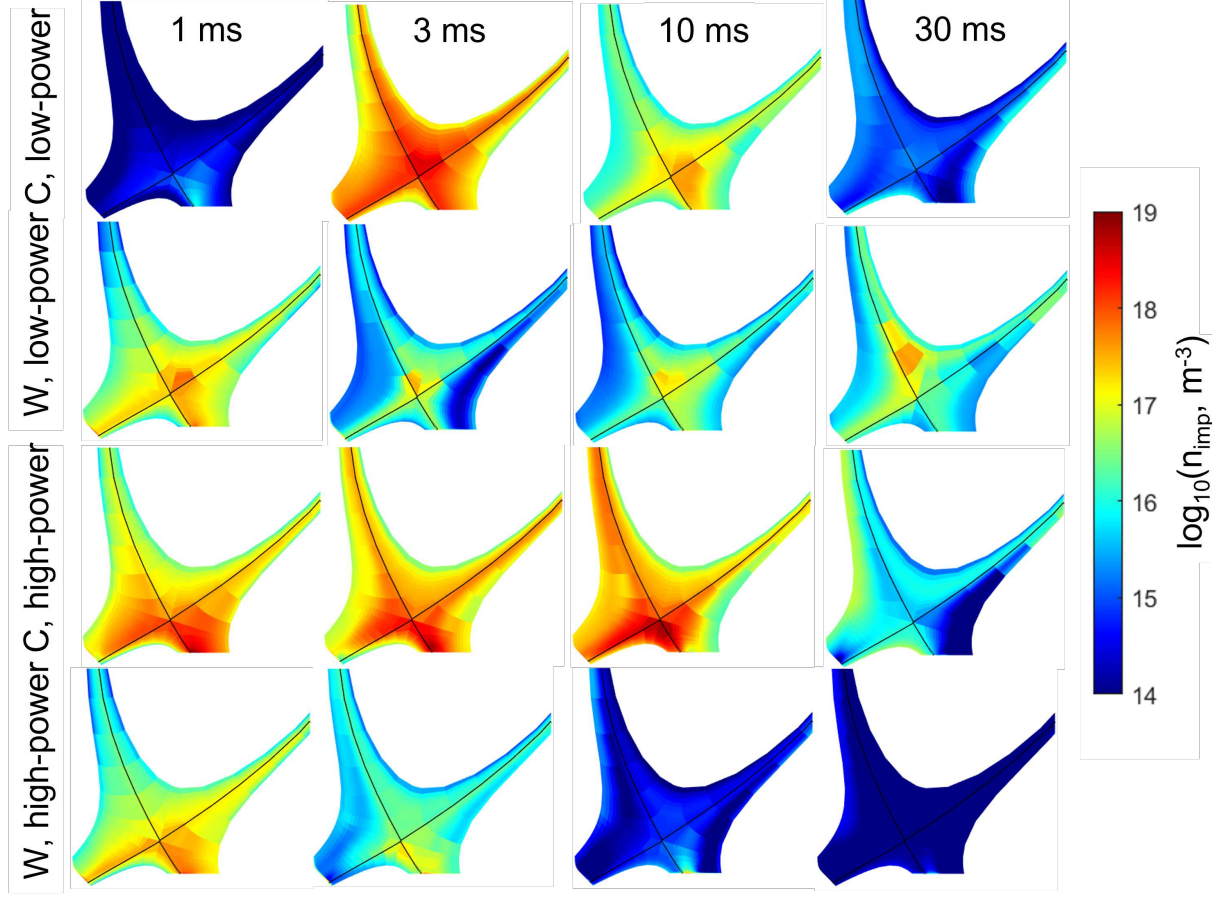
This is the author's peer reviewed, accepted manuscript. However, the online version of record will be different from this version once it has been copyedited and typeset.

PLEASE CITE THIS ARTICLE AS DOI: 10.1063/5.0144529



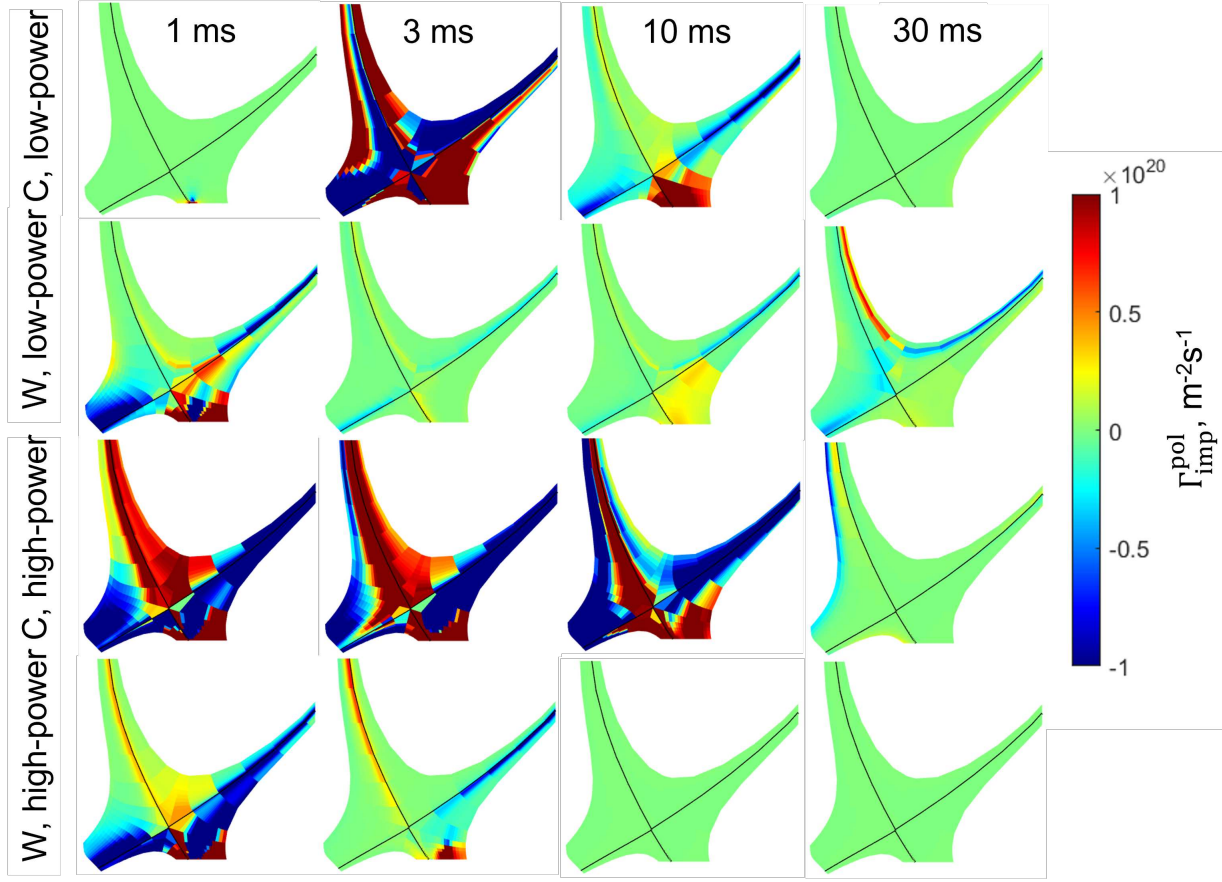
This is the author's peer reviewed, accepted manuscript. However, the online version of record will be different from this version once it has been copyedited and typeset.

PLEASE CITE THIS ARTICLE AS DOI: 10.1063/1.50144529



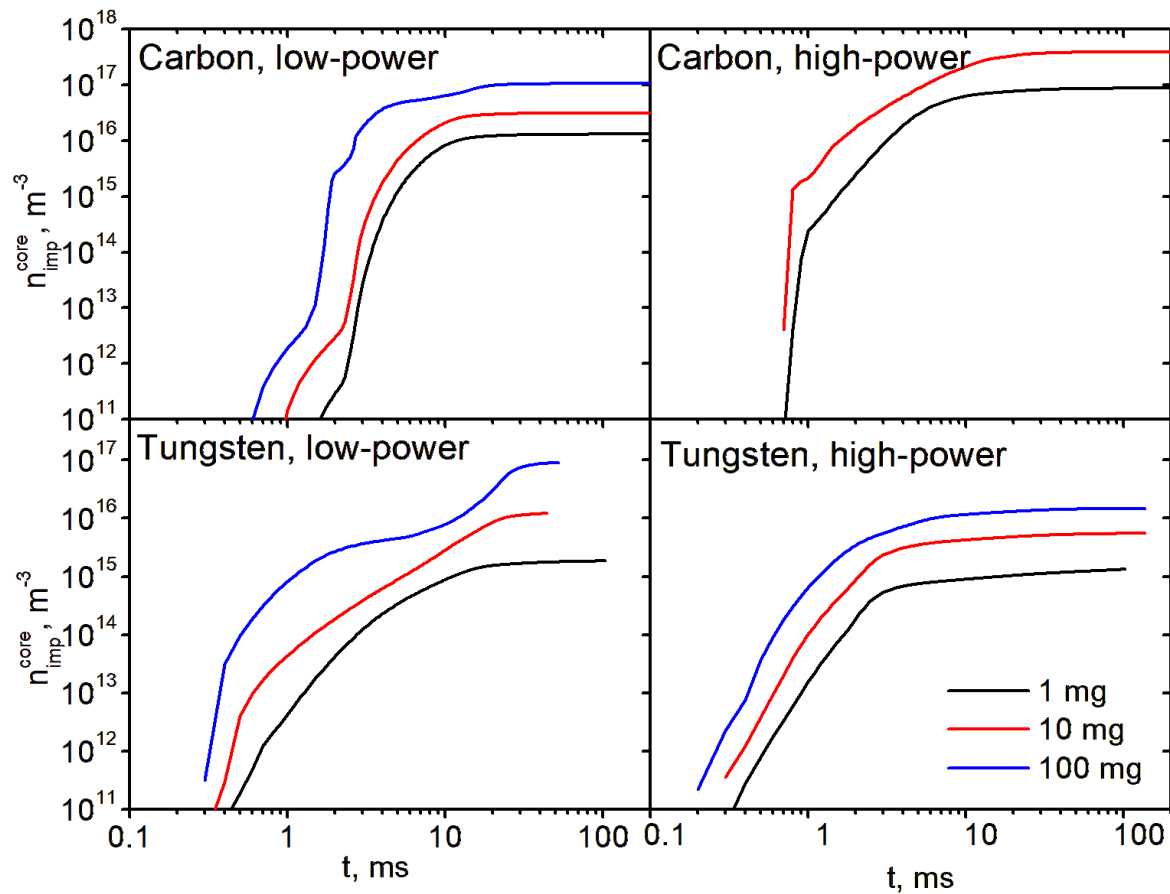
This is the author's peer reviewed, accepted manuscript. However, the online version of record will be different from this version once it has been copyedited and typeset.

PLEASE CITE THIS ARTICLE AS DOI: 10.1063/5.0144529



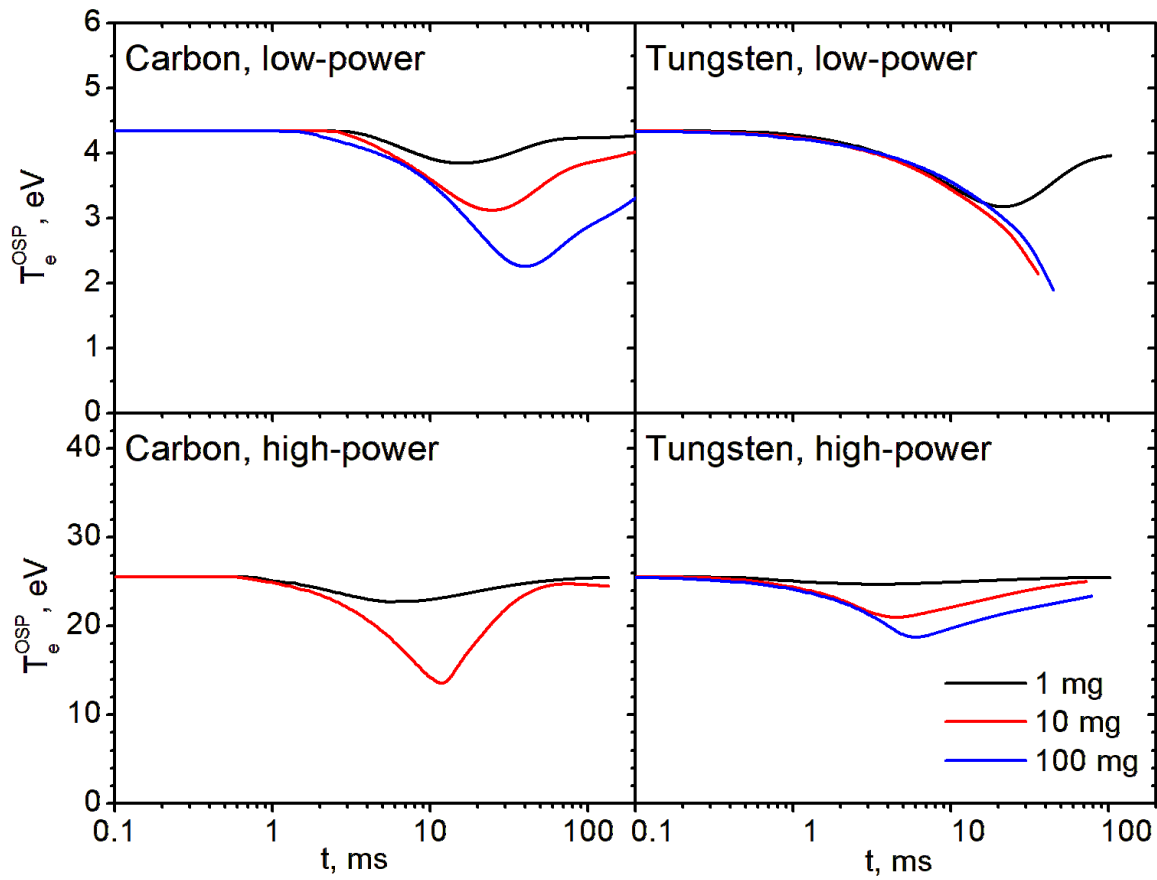
This is the author's peer reviewed, accepted manuscript. However, the online version of record will be different from this version once it has been copyedited and typeset.

PLEASE CITE THIS ARTICLE AS DOI: 10.1063/5.0144529



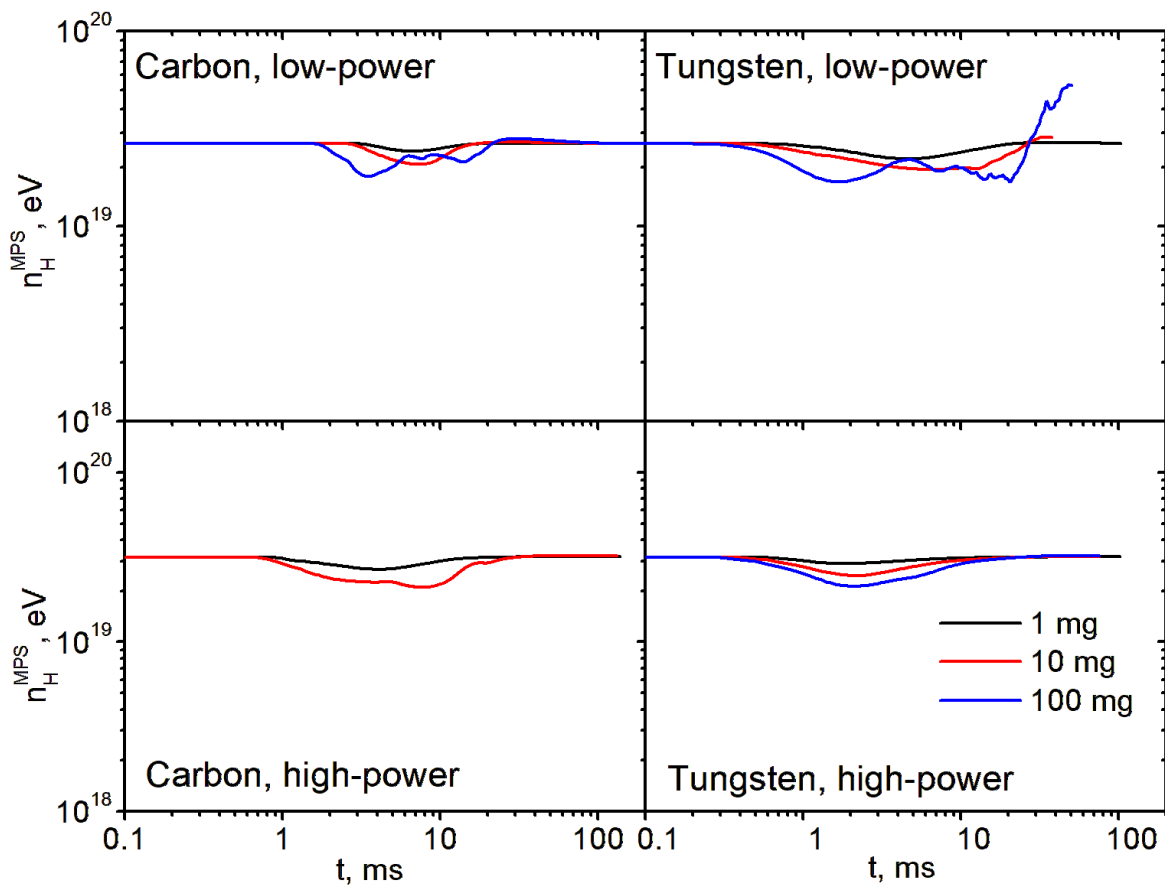
This is the author's peer reviewed, accepted manuscript. However, the online version of record will be different from this version once it has been copyedited and typeset.

PLEASE CITE THIS ARTICLE AS DOI: 10.1063/5.0144529



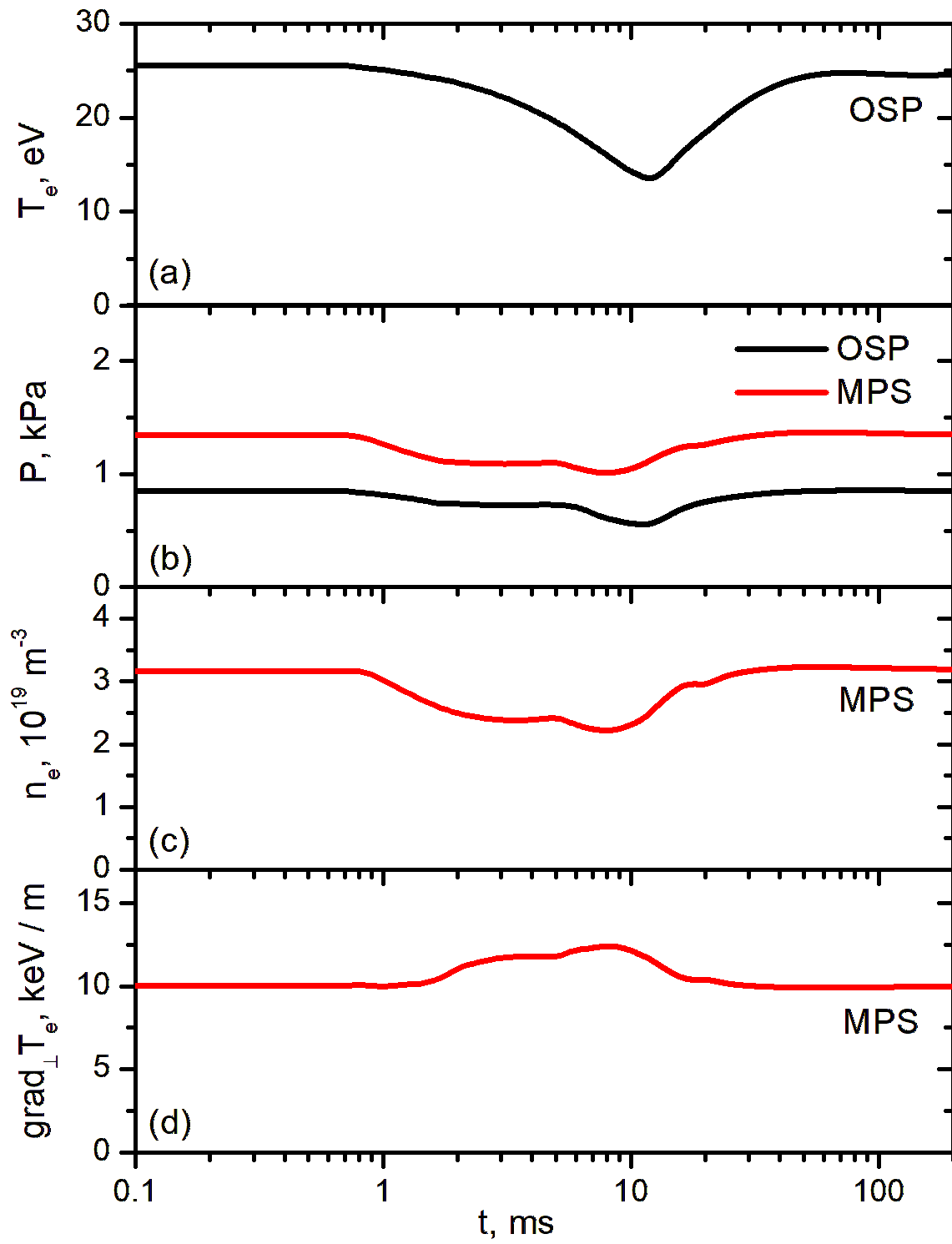
This is the author's peer reviewed, accepted manuscript. However, the online version of record will be different from this version once it has been copyedited and typeset.

PLEASE CITE THIS ARTICLE AS DOI: 10.1063/1.50144529



This is the author's peer reviewed, accepted manuscript. However, the online version of record will be different from this version once it has been copyedited and typeset.

PLEASE CITE THIS ARTICLE AS DOI: 10.1063/5.0144529



This is the author's peer reviewed, accepted manuscript. However, the online version of record will be different from this version once it has been copyedited and typeset.

PLEASE CITE THIS ARTICLE AS DOI: 10.1063/5.0144529

